Diversity of collective migration patterns of invasive breast cancer cells emerging during microtrack invasion

Ruchuan Liu,[1,*] Kena Song,[1,*] Zhijian Hu,[1] Wenbin Cao,[1] Jianwei Shuai,[2] Shaohua Chen,[3] Hanqing Nan,[3] Yu Zheng,[4] Xuefeng Jiang,[5] Hongfei Zhang,[5] Weijing Han,[6] Yong Liao,[7] Junle Qu,[8] Yang Jiao,[3,4,†] and Liyu Liu[1,†]

[1]*Chongqing Key Laboratory of Soft Condensed Matter Physics and Smart Materials, College of Physics, Chongqing University, Chongqing 401331, China*

[2]*Department of Physics, Xiamen University, Xiamen 361005, China*

[3]*Materials Science and Engineering, Arizona State University, Tempe, Arizona 85287, USA*

[4]*Department of Physics, Arizona State University, Tempe, Arizona 85287, USA*

[5]*Hygeia International Cancer Hospital, Chongqing 401331, China*

[6]*Shenzhen Shengyuan Biotechnology Co. Ltd., Shenzhen 518000, China*

[7]*Institute for Viral Hepatitis, Department of Infectious Diseases, Second Affiliated Hospital, Chongqing Medical University, Chongqing 400331, China*

[8]*Key Lab of Optoelectronic Devices and Systems of Ministry of Education/Guangdong Province, College of Optoelectronic Engineering, Shenzhen University, Shenzhen 518060, China*

(Received 10 December 2018; revised manuscript received 18 April 2019; published 6 June 2019)

Understanding the mechanisms underlying the diversity of tumor invasion dynamics, including single-cell migration, multicellular streaming, and the emergence of various collective migration patterns, is a long-standing problem in cancer research. Here we have designed and fabricated a series of microchips containing high-throughput microscale tracks using protein repelling coating technology, which were then covered with a thin Matrigel layer. By varying the geometrical confinement (track width) and microenvironment factors (Matrigel concentration), we have reproduced a diversity of collective migration patterns in the chips, which were also observed *in vivo*. We have further classified the collective patterns and quantified the emergence probability of each class of patterns as a function of microtrack width and Matrigel concentration to devise a quantitive "collective pattern diagram." To elucidate the mechanisms behind the emergence of various collective patterns, we employed cellular automaton simulations, incorporating the effects of both direct cell-cell interactions and microenvironment factors (e.g., chemical gradient and extracellular matrix degradation). Our simulations suggest that tumor cell phenotype heterogeneity, and the associated dynamic selection of a favorable phenotype via cell-microenivronment interactions, are key to the emergence of the observed collective patterns *in vitro*.

DOI: 10.1103/PhysRevE.99.062403

I. INTRODUCTION

The capacity for invasion and metastasis makes cancer a life-threatening disease. Invasive tumor cells can detach from the primary tumor mass, penetrate basement membranes and endothelial walls, and invade the vessel lumen. The dissemination of cancer cells to distant organs and the development of secondary tumors usually leads to fatal outcomes for patients [1]. During collective invasion, tumor cells can form and maintain a dynamic cluster with different morphologies. Various collective invasion patterns have been observed in pathological samples, such as in biopsies of oral squamous cell carcinomas, ductal breast carcinomas, and rhabdomyosarcomas [2,3]. A preponderance of previous studies focused on the migration behavior of individual tumor cells has provided significant insights into single-cell-based cancer invasion mechanisms [4,5]. However, it is generally believed that collective invasion can be more aggressive and efficient than single-cell invasion [6,7]. Extensive experimental [8–11] and computational [12–14] investigations have been carried out to reveal possible mechanisms for the emergence of various collective patterns, including identification of pathways important for the regulation of cell adhesion and cytoskeletal dynamics [4,5,15] as well as understanding of the interplay of cancer cells with fibroblasts, endothelial cells, and/or macrophages [16–20]. Recently, Friedl *et al.* summarized a systematic classification scheme for different dissemination modes of cancer cells based on the characteristic morphology of collective invasion patterns [3]. Although the summary was based on years of pathology study, the classification was mainly based on qualitative observations and no quantitative schemes were given.

Many studies have suggested that aside from intrinsic cell properties and cell-cell interactions, the heterogeneous tumor microenvironment also plays a crucial role in giving rise to collective cell invasion [21–24]. For instance, the influence of the microenvironment on the metastasis of cancer cells via the regulation of cell adhesion and migration has been investigated both *in vivo* and *in vitro* [25,26]. Moreover,

*These authors contributed equally to this paper.

†Corresponding authors: lyliu@cqu.edu.cn; yang.jiao.2@asu.edu

novel *in vitro* experiments have been developed that mimic the heterogeneous tumor microenvironment *in vivo* and thus enable quantitative analysis of the effects of the tumor microenvironment, including geometrical confinement, extracellular matrix (ECM) density, hypoxia, pH levels, and nutrient gradient.

In the past decade, a "migration-on-track" technique has been developed that allows one to investigate cell migration under the influence of contact guidance and geometrical confinement [27–30], as well as cancer invasion and metastasis, in a confined environment [31] using microfabricated substrates with controlled physical and morphological features [32–39]. For example, a commonly used class of substrates includes microchips containing high-throughput microscale tracks. In most previous "migration-on-track" studies, the heterogeneous tumor microenvironment was not explicitly considered or mimicked. Since the microenvironment and the associated tumor-environment interactions can play an important role in collective tumor cell invasion, it is highly desirable to develop microchip systems that incorporate controllable microenvironment models. This enables one to systematically investigate the influence of varying microenvironmental factors on collective cell behaviors.

In this work, we have designed and fabricated high-throughput microfluidics chips using the soft-lithographic method [40], which allows us to systematically investigate collective pattern formations during tumor cell migration. This set allows us to carry out many "single-track" experiments in parallel. Recently, it was shown that collagen fibers could guide cancer cell invasion into the ECM [41]. The patterned microtracks are further covered by a thin layer of Matrigel with different concentrations instead of collagen. The Matrigel layer is expected to be more uniform at the cellular level, as well as to avoid the guiding effect of collagen on cancer cell migration. In the subsequent discussion, we will occasionally refer to the Matrigel layer as "ECM" for simplicity, while it is important to note that Matrigel is not a component of the ECM, but just to mimic the ECM in our *in vitro* experiments. In addition, by varying the Matrigel concentrations, we could mimic the effects of the microenvironment with different levels of stiffness. The control experiments illustrated that the network structure that Matrigel possesses is more uniform and stable than collagen. By varying the microtrack width (geometrical confinement) and Matrigel concentration (microenvironment), we have reproduced a diversity of collective migration patterns observed in tumor invasion *in vivo*. We have further quantitatively classified the invasion patterns into four major categories, including stream, blunt tip, cone tip, and lumen. We then quantified the emergence probability of each class of patterns as a function of microtrack width and Matrigel concentration. This allowed us to construct a "collective pattern diagram," which shows the correlation between the emergence of various collective migration patterns and the geometric or microenvironment factors. In addition, we utilized the cellular automaton (CA) simulation to explore the mechanism of the collective pattern formation and the role of the microenvironment. Finally, we discuss the relationship between the microenvironmental factors and cell phenotype heterogeneity in giving rise to various collective migration patterns.

II. METHODS

A. Clinical diagnostic criteria

The clinical specimens, 60 slices and diagnostic reports, were collected from 60 breast cancer patients with pathological grades 2 or grades 3 supported by the Hygeia International Cancer Hospital. We selected 2210 fronts from the slices for subsequent analysis. Pathological diagnoses of the cancer cells boundary and cell clusters were made by two pathologists independently following clinical diagnostic criteria according to the 2012 WHO classification [42–44]. Typical samples of the four patterns in slices are shown in Fig. 2(a) below, in which the morphology of the fronts is outlined by the red line. The stream pattern is defined by the cancer cells invading to the ECM one by one as a chain; only one cell leading the collective cells to invade is defined as the cone-tip pattern; more cells leading the collective cells are defined as the blunt-tip pattern; and the front part of the collective cells with a cavity is defined as the lumen pattern.

B. Solution preparation

The materials used in this study, including coverslips, silicon wafers, and all of the chemicals, were purchased from Sigma-Aldrich (Milwaukee, WI, USA) unless otherwise stated.

For the acrylamide/*N*, *N*-methylenebis(acrylamide) (AAM/BIS) solution, 0.15 g/ml acrylamide (AAM) (>9.9%, A3553, powders), 1.5 mg/ml *N*, *N*-methylenebis(acrylamide) (BIS) (99.5%, MW: 154.17), and 0.0545 g/ml benzophenone (99+%, 427 551) were dissolved in 20 ml acetone. For the polyethylene glycol (PEG)/BIS solution, 0.03 g/ml PEG (81 280, MW: 8500–11 500), 0.045 g/ml BIS, and 0.0545 g/ml benzophenone were dissolved in 20 ml methanol (9.99%, 34 860).

C. Track preparation for cell migration

To investigate the effects of the ECM and limited space (geometrical confinement) on the collective migration of malignant tumor cells, we created an engineered *in vitro* microtrack-based microenvironment (shown in Fig. 1), following a procedure modified from the one reported by Tourovskaia *et al.* [40].

The coverslips were rinsed in turn using a detergent (50% Decon 90) and deionized water, cleaned with oxygen plasma, rinsed again with deionized water, and finally blow-dried using nitrogen. Then the clean coverslips were incubated in a solution of allyltrichlorosilane (ATC) (MW: 175.52, 107 778) and toluene (1:79 in volume) for 5 min, followed by rinsing in turn with pure toluene, acetone, and deionized water. The ATC-modified coverslips were cured at 90 °C for 1 h and then put into the AAM/BIS solution for 5–10 min. After exposure to UV light (64 W UV lamp), a white gel between the coverslip and the Petri dish bottom formed and solidified in ∼7 min. Here cross-linked poly-AAM (PAMM) was formed by UV-initiated polymerization with BIS. Again the coverslips were rinsed with acetone and deionized water in turn to remove the unbounded gel, and then blow-dried using nitrogen. Finally, the coverslips were put in the PEG/BIS solution with the grafted side face to the bottom and exposed

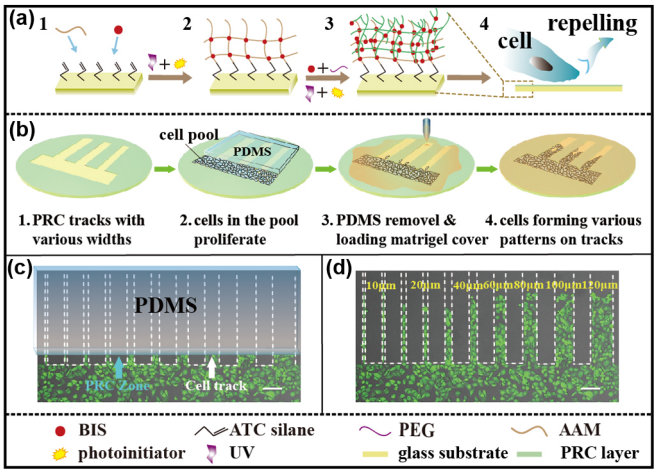

FIG. 1. Illustration of the migration-on-track experiments. (a) The procedure to synthesize AAM PRC on glass substrates: An allyltrichlorosilane (ATC)-grafted glass substrate (a1) is further modified by AAM and BIS via photopolymerization under UV; subsequently the formed gridlike structure on the substrate (a2) is again cross-linked with PEG via BIS by photopolymerization; finally, the IPN structure (a3) is formed; (a4) the modified surface repels the cell from adhesion. (b) Schematic illustration of the experimental procedures. The tracks with various widths were established on the microchip (b1), and then cells were seeded in the pool for incubation. Meanwhile a PDMS block was applied to the tracks to prevent the cells from running into the tracks (b2). Matrigel with a specific concentration was dropped onto the tracks to mimic the variations of ECM *in vivo*, when the pool was filled by cells due to proliferation (b3). Cells invaded the tracks and exhibited various migration patterns (b4). (c) Before the migration experiment, the cells were held in the pool with a PDMS block on the tracks. (d) A typical fluorescence image by confocal microscopy showing a snapshot of the tumor cells migrating on microtracks with varying widths. The MDA-MB-231 cells marked with green fluorescent protein in panels (c) and (d) were obtained from China Infrastructure of Cell Line Resources (Beijing, China). The scale bar = 100 μm.

to UV light for ∼7 min to form the interpenetrating polymer network (IPN) between PAMM and PEG via polymerization with BIS. The IPN layer is highly biocompatible and able to prevent protein binding to the surface due to the extremely hydrophilic nature and low interfacial free energy of AAM. Thus, the PRC surface can prevent cell adhesion. The PRC layer was 50–80 nm in thickness. The PRC-coated coverslips were cleaned in turn using methanol, acetone, and deionized water, and finally blow-dried [Fig. 1(a)].

To create "microtracks" on the PRC-coated coverslips, photolithography was used. The detailed photolithography procedure is described in the Supplemental Materials Fig. S1 [45].

D. Invasion-on-tracks experiments

Before carrying out the cell migration experiments, the tracks were covered with a PDMS block (Dow Corning, MI, USA; cured at 10:1 with elastomer), while metastatic breast cancer cells were cultured in the groove next to the tracks. The malignant MDA-MB-231 breast cancer cell line marked with green fluorescent protein was obtained from the China Infrastructure of Cell Line Resources (Beijing, China). The cell culture was carried out in Dulbecco's Modified Eagle Medium (Corning, NY, USA) with 10% fetal bovine serum (Corning) and 1% penicillin-streptomycin (Corning) for 24 h, when the cancer cells filled the groove [Fig. 1(b)]. Then, upon the removal of the PDMS block, the track regions of the coverslip chip were covered by a ∼200-μm-thick Matrigel layer, one of the major components in ECM. The Matrigel layer also provided an *in vitro* microenvironment with varying density, pore size, and stiffness via the use of differing concentrations (30%, 60%, 90%, and 100%, diluted by buffer). The widths of microtracks were also varied in the experiment (10 μm, 20 μm, 40 μm, 60 μm, 80 μm, 100 μm, 120 μm, 140 μm, 160 μm, 180 μm, and 200 μm) to investigate the effects of geometrical confinement. Once the PDMS block was removed, the cells were able to migrate on the Matrigel-covered microtracks. Subsequently, the chip was placed in the 37 °C incubator and the cell migration behaviors were continuously monitored for ∼72 h with 12 h per snapshot, during which steady migration patterns formed. In most cases, only one dominant steady-state migration pattern was observed for specific microtracks of small and intermediate width. However, multiple steady collective patterns simultaneously occurred on the wide microtracks. In such cases, all of the different patterns observed for the specific track width were considered when obtaining the statistics (e.g., probability of occurrence of different patterns as a function of track width). The probability of the four patterns is the observed via a normalization procedure described in detail below.

E. Imaging methods

The images of collective migration patterns were obtained using a Nikon Ti-E bright field microscope with 40× amplification, and a Leica TCS SP8 confocal microscope through a green fluorescent channel excited at 488 nm with 100× amplification. The patterns on the tracks *in vitro* were recognized by independent encoding in Matlab (MathWorks, MA, USA). A detailed definition of the quantitative classification is shown in Table I.

F. Quantitative classification scheme for various collective migration patterns

In the *in vitro* experiments and numerical simulations, it was observed that the evolution of the migration pattern, i.e., the morphology of the migration front, was dynamic at the beginning but reached a quasi-steady state after ∼24 h. In other words, the "phenotype" of the migration front remained stable for a relatively long period (∼40 h). Based on the categorization by Friedl *et al.* [3] and the images of the cancer-tissue slices, we focused on four types of commonly seen collective migration patterns (i.e., steady-state migration front morphology): stream, cone tip, blunt, and lumen. These patterns are quantitatively defined based on their geometric properties as described below. The definitions of the geometrical parameters d, d_0, θ, θ_0, S, and S_0 are given in Table I.

We noted that the parameter values for d_0, θ_0, and S_0 were determined such that different patterns could be robustly

TABLE I. Quantitative classification scheme of collective migration patterns.

Pattern type	Characteristics	Quantification scheme
Stream	Cancer cells migrate in a single line	The width of the migration front d is smaller than $2 \times d_0$, i.e., $d \leqslant 2 \times d_0$ where $d_0 \sim 15\,\mu$m is the linear size of a cell
Cone tip	Cancer cells migrate in a group with a conelike front	The angle θ of the migration front tip is smaller than a prescribed threshold θ_0, i.e., $\theta < \theta_0 = \tan^{-1}(0.6)$ and the front width $d > 2d_0$
Blunt tip	Cancer cells migrate in a group with a blunt and flat front	The front tip angle $\theta \geqslant \theta_0$, and the front width $d > 2d_0$
Lumen	Cancer cells migrate in a group with a migration front containing a small cavity	The area of the cavity S in the migration front is greater than the area of one and a half cells $S_0 \sim 1072\,\mu\text{m}^2$, i.e., $S \geqslant S_0$

classified despite the cell-level fluctuations (see Ref. [45] for details how these parameters are determined). With the quantitative classification scheme, the probability of occurrence for each class of collective patterns can be obtained for various track widths and Matrigel concentrations. Specifically, the occurrence (or emergence) probability of a particular pattern for a given track width ω and Matrigel concentration ρ was computed by first counting and summing the total number of different patterns observed for this set of microenvironment parameters [10,17,20,30], i.e., $N(\omega,\ \rho) = \sum N_{\text{p}}[\omega,\ \rho]$, where N_{p} is the number of pattern "p" (i.e., p = "S" for stream, "B" for blunt, "C" for cone, and "L" for lumen) observed. The probability for a particular collective pattern is then calculated as $\phi_{\text{p}}(\omega,\ \rho) = N_{\text{p}}/N$. A probability map, which correlates the probability of occurrence for each pattern with the geometrical confinement (i.e., track width) and microenvironmental factors (i.e., Matrigel concentration), can subsequently be obtained by interpolating the discrete experimental data points using the Gaussian expansion. Finally, a "collective pattern diagram" is constructed that highlights the dominant collective migration pattern (based on the occurrence probability) for a given set of track width and Matrigel concentrations.

G. Cellular automaton model for invasive tumor cells

Here we present the algorithmic details of our CA model for the system. The CA model developed here is based on a previous model developed by the authors for simulating invasive tumor growth [46–49]. In the model, the simulation domain was a two-dimensional rectangular region with width ω and length H. Different track widths ($\omega = 25$, 40, 60, 75, 100, 120, 150, 180, and 200 μm) and a single length ($H = 800\,\mu$m) were used in the simulations. The simulation domain was discretized into irregular polygons using a Voronoi tessellation based on a disordered hard circular disk packing generated using random sequential addition. The average linear size of the Voronoi polygons was $\sim 15\,\mu$m, which is consistent with the characteristic size of a cell. The tumor cells were allowed to enter the domain from the bottom and leave from the top. In our simulations, a steady state (or stable) collective migration pattern was typically established long before the cells reached the top boundary of the simulation domain, which is consistent with the experimental observations.

In the CA model, each Voronoi polygon, which is also referred to as an "automaton cell" or "CA polygon," can represent either a tumor cell or a region of Matrigel. In the beginning of the simulation, the entire simulation domain was covered with Matrigel with a density ρ in (0, 1); i.e., all of the CA polygons represent Matrigel. We note that the Matrigel density used here was a model parameter that characterized the relative resistance for cell migration, which is different from the experimental counterpart and does not possess a physical unit. In our simulations, we used the four distinct density values $\rho = 0.25$, 0.5, 0.75, and 1.0. Then the tumor cells were allowed to continuously enter the simulation domain from the bottom boundary. Time was discretized into steps consistent with a typical cell migration cycle. During each time step, all of the tumor cells were checked for possible migration and position updates based on the following CA rules:

(1) Each tumor cell possesses an intrinsic Matrigel degradation ability γ in (0, 1), and motility μ in (1, $\mu_{\max}$), and we used $\mu_{\max} = 5$ in our simulations. Specifically, during a migration cycle, a tumor cell will make μ attempts to migrate into a neighboring CA polygon filled with Matrigel with density ρ. For each attempt, the Matrigel is degraded by a certain amount that is characterized by the reduced ρ by γ. If the Matrigel is completely degraded within μ attempts ($\rho < \gamma\mu$), the cell will migrate into the selected CA polygon and the density of its original CA polygon is set to 0; otherwise, the cell remains in its current CA polygon, and the density of the selected neighboring polygon is updated as

$$\rho = \rho - \gamma\mu. \tag{1}$$

(2) The direction of migration of a tumor cell is determined by three factors: (1) chemotaxis, (2) local Matrigel density, and (3) cell-cell adhesion. Specifically, the chemotaxis is always along the direction of the track direction and is specified by the unit direction $\mathbf{C_0}$. Let the unit direction vector point from the current CA polygon to the neighbor polygon J, denoted by $\mathbf{e}_J$, then the CA polygon (filled with Matrigel) that the tumor cell attempts to migrate into is the one that maximizes the following quantity:

$$\max_J \left\{ \left(\frac{\rho_{\max} - \rho_J}{\rho_{\max} - \rho_0} \right) \left(\mathbf{C}_0 + f \sum_K \mathbf{e}_K \right) \cdot \mathbf{e}_J \right\}, \tag{2}$$

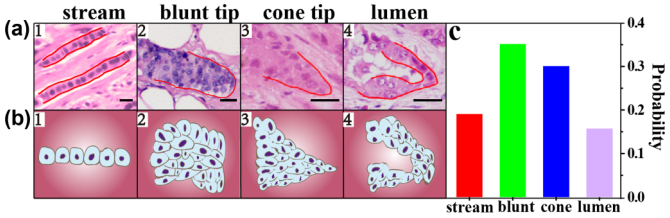

FIG. 2. Categorization and clinical pathological slice probability statistics of the most commonly seen collective migration patterns of invasive tumor cells based on the analysis of pathological slices of breast cancers: (a) images of clinical slices and (b) corresponding cartoons showing four types of collective patterns—(1) stream, (2) blunt tip, (3) cone tip, and (4) lumen—and (c) the probability of the four types of patterns in the clinical pathological slices from 60 patients.

where $\mathbf{e}_K$ is the unit vector pointing to neighboring CA polygon occupied by tumor cells, and f is an effective force parameter that characterizes the net adhesive force due to neighboring tumor cells, ρ_J is the Matrigel density in the CA polygon J, and $\rho_{\max}$ and ρ_0 are, respectively, the maximal and minimal Matrigel density in the system.

(1) New tumor cells can continuously enter the simulation domain if there are unoccupied CA polygons on the domain boundary.

We note that Eq. (2) implies that the migrating cells take the path with least resistance, which is achieved in the simulations by moving to a neighboring CA polygon with the smallest ECM density ρ_J [i.e., by maximizing $(\rho_{\max} - \rho_J)/(\rho_{\max} - \rho_0)$. In addition, the cells tend to move along the chemotaxis direction $\mathbf{C_0}$ and are affected by the neighboring tumor cells due to cell-cell adhesion.

For each new simulation, a tessellation based on a different random-sequential-addition packing will be used. In addition, we do not explicitly specify any CA rules to force neighbor connections to be maintained during the simulations. The apparently stable patterns produced by the model (see the Results section) can consist of cells constantly switching positions. We believe these patterns are emergent and stabilized by cell-ECM interactions (e.g., least-resistant path selection) and cell-cell adhesion. Finally, we note that cells *in vivo* can squeeze through the holes in ECM, and this mechanism is not explicitly considered in the current CA model.

III. RESULTS AND DISCUSSION

A. Clinical diagnostic statistics

In this study, we observed the various collective migration patterns (i.e., the morphology of collectively migrating cell groups/clusters) from 60 pathological sections with 2210 fronts from different breast cancer patients. The collective patterns of cancer cells are identified in the pathological images. The identified collective patterns match the collective dissemination modes of invasive tumor cells proposed by Friedl *et al.* [3] In addition, we categorized the most commonly observed patterns into four types: stream, blunt tip, cone tip, and lumen, as shown in Fig. 2(a).

The distribution of the four patterns is shown in Fig. 2(c). Results show that in the patients with pathological stage 2 and 3 cancer, the cancer cells invaded mostly via blunt tip, the percentage of which was more than 35%. The percentage of the cone tip, stream, and lumen was 29.7%, 19.3%, and 15.5%, respectively. As the sample size of 60 is still quite limited, we expect that the ratio *in vivo* could vary. Nevertheless, how these patterns form *in vivo* remains unclear. We emphasize that the histological data can provide only snapshots of collective patterns, which might form during a collective migration process. However, the snapshots alone are not sufficient for us to conclude whether these patterns were dynamic (composed of migrating cells) or just stable static patterns. In this work, we hypothesize that these collective patterns could emerge during a collective migration process regulated by the cell-microenivornment interactions. We will test this hypothesis and study the formation mechanism of the four patterns using carefully designed and implemented *in vitro* experiments and computational modeling (see Methods). Meanwhile, the detailed definition of the four patterns is provided in Table I. The results of the *in vitro* experiments are given next.

B. Quantification and classification of collective migration patterns

To mimic the geometric confinement of *in vivo* cancer invasion, the protein repellent coating (PRC) technique (see Fig. S4 [45]) was employed to create microtracks with various widths on glass cover slices [40] (see Methods). In addition, a layer of Matrigel (including 56% laminin, 31% collage type IV, and 8% entactin, which are the main components of the extracellular matrix) was used to cover the tracks [Fig. 1(b)] to mimic the effects of the *in vivo* microenvironment. The concentration of Matrigel was designed at 30%, 60%, 90%, and 100% to mimic the heterogeneity of the ECM, which shows different pore sizes and stiffness around the tumor cells. It is noted that the actual tumor microenvironment is highly complex and heterogeneous, containing collagen, stromal cells, and vascular structures. The simple Matrigel layer with varying concentrations clearly cannot reproduce the full spectrum of the effects of such complex ECM *in vivo*. However, experimentally, a similar layer of collagen could barely be achieved. Compared to collagen, the network structure of Matrigel is more uniform at the cellular level and can provide resistance for migrating tumor cells, which is a key factor for the emergence of collective migration patterns.

In the following migration-on-track experiments, the metastatic breast cancer cells (MDA-MB-231) were first cultured in the pool on the PRC patterned glass slide [Fig. 1(b1)]. A PDMS block was used to cover the tracks until the pool was filled with cells [Fig. 1(b2)]. Upon removal of the PDMS block, a layer of Matrigel was immediately dropped onto the slide to cover the tracks for cell migration, as is shown in Figs. 1(b3) and 1(b4) (see Methods for details). Using this approach, the microtracks with 10 μm, 20 μm, 40 μm, 60 μm, 80 μm, 100 μm, 120 μm, 140 μm, 160 μm, 180 μm, and 200 μm were integrated into a single microchip for migration-on-track studies [Figs. 1(c) and 1(d)]. The experiment was repeated 60 times with the same conditions for data collection. The number of occurrences observed per migration phenotype

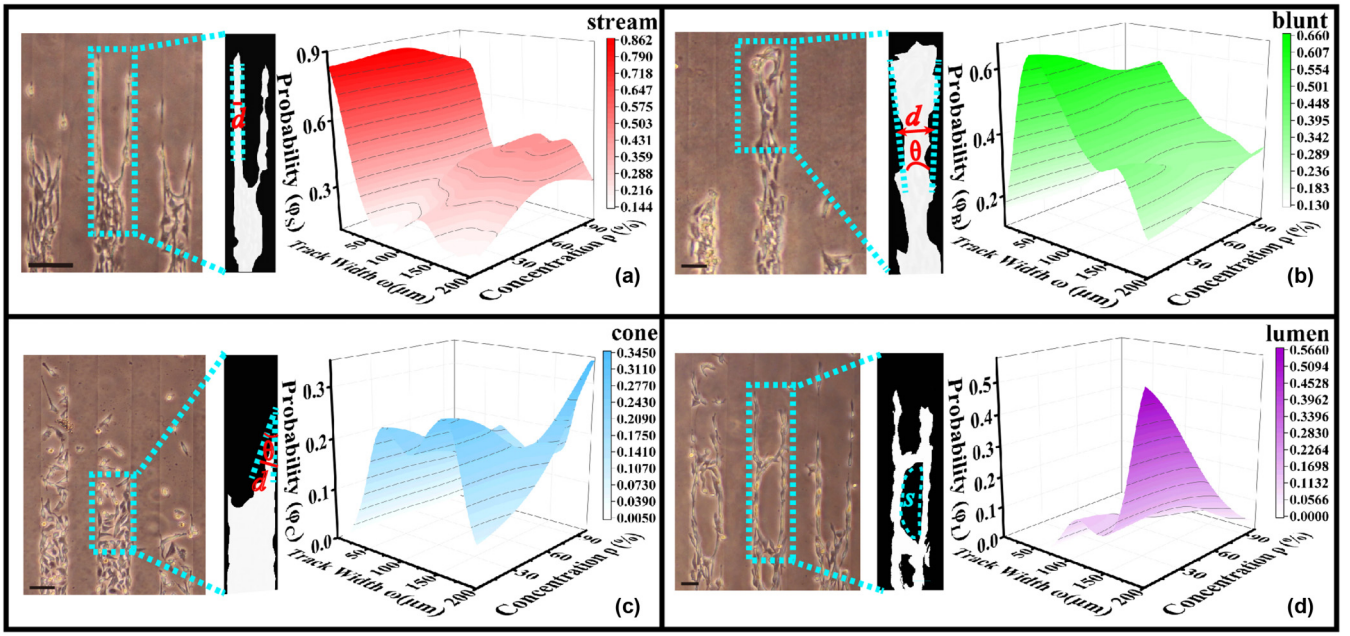

FIG. 3. Quantitative analysis of different collective migration patterns emerging in the *in vitro* experiments with 60 repetitions, which resemble the collective patterns observed *in vivo*. The left column is the steady-state collective migration patterns from the migration-on-track experiments, followed by an illustration of the quantitative analysis of the patterns: (a) a stream pattern (the migration front width $d < 2d_0$); (b) a blunt-tip pattern (the front angle $\theta > \theta_0$, and $d > 2d_0$); (c) a cone-tip pattern ($\theta < \theta_0$ and $d > 2d_0$); and (d) a lumen pattern (the area of the cavity $S > S_0$, which is roughly the area one and a half cells). Here $\tan\theta_0 = 0.6$, $d_0 = 15\,\mu$m, and $S_0 \sim 1072\,\mu\text{m}^2$. The right column is the corresponding color map for the probability of emergence for the four types of patterns vs track width ω and Matrigel concentration ρ, in which dark colors indicates higher probability. The scale bar shown is $100\,\mu$m.

per track width varied in a range of 10 to 45; the probability distributions are shown in Fig. 3.

Our high-throughput microchips enabled us to systematically investigate the migration behaviors of invasive breast cancer cells (MDA-MB-231) and the emergence of various collective migration patterns. This was achieved by varying the geometrical confinement (i.e., track widths) and ECM density and stiffness (i.e., Matrigel concentrations), which are typically encountered during *in vivo* cancer invasion. Indeed, we observed different steady collective migration patterns of MDA-MB 231 cells on the microtracks with different width and Matrigel concentrations. These *in vitro* patterns resemble the previously identified four types of invasion patterns observed *in vivo* (Fig. 2). Furthermore, we have confirmed, using confocal microscopy, that the tumor cells only migrate on the track and do not invade into the Matrigel in the vertical direction (see supplemental movie 2 [45]). This observation demonstrates the capability and feasibility of our migration-on-tracks chips for collective cell migration study.

We further quantified each of the observed patterns and classified them into one of the four categories identified (see Methods for technical details). Then the probability of emergence (or occurrence) ϕ of each type of pattern as a function of track width ω and Matrigel concentration ρ was computed. This allowed us to derive a "probability map" for each type of pattern (see Fig. 3) via the interpolation of the statistics obtained from discrete values of track width and Matrigel concentration (see Methods). These probability map, in which the emergence probability of a specific pattern associated with specific track width ω and Matrigel concentration ρ is indicated by the corresponding color scale, illustrates the dependence of invasion dynamics on the two microenvironmental factors. The invasion patterns are measured and the scattered individual cells are excluded because they do not contribute to the collective patterns. According to these maps, the characteristics and trends of the four types of patterns are summarized as follows:

(1) The stream patterns emerged for all values of ω and ρ [Fig. 3(a)]. The emergence probability of stream patterns φ_S approached unity ($\sim$100%) for the narrow tracks ($\omega < 25\,\mu$m), decreased rapidly at $\omega \sim 40\,\mu$m, and slightly increased again after the minimum of φ_S ($\sim$14.4%) at $\omega \sim 55\,\mu$m, and then plateaued ($\sim$40%) for higher Matrigel concentration $>$ 50% for wider tracks $> 80\,\mu$m.

(2) Both the blunt-tip and cone-tip patterns [Figs. 3(b) and 3(c)] emerged at $\omega \sim 40\,\mu$m. The probability for the blunt patterns φ_B increased rapidly to $\sim$60% at $\omega \sim 50\,\mu$m and then slowly and slightly decreased when ω was further increased. The probability of the cone-tip pattern φ_C rapidly increased to 25% for low Matrigel concentration $\rho < 45\%$. For very large track width, e.g., $\omega \sim 180\,\mu$m, φ_C showed a peak $\sim$34% with high Matrigel concentration $>$90%.

(3) The lumen pattern emerged on tracks with $\omega > 80\,\mu$m [Fig. 3(d)], which is the critical width for cells to form a connected sheet and enclose a cavity. In addition, the emergence probability of lumen patterns φ_L increased to $\sim$56% gradually with the increasing of ω and the decreasing of ρ.

The movies of the four-pattern probability distributions are shown in the supplemental movies 4–7 [45].

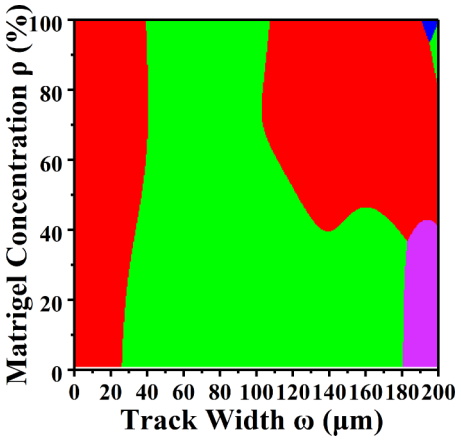

FIG. 4. Collective pattern diagrams from migration-on-track experiments. Four distinct pattern regions are identified based on experimental data. The red, green, blue and purple regions represent the stream, blunt-tip, cone-tip, and lumen patterns, respectively.

C. Transition of the dominant collective pattern as microenvironment varies—The collective pattern diagram

We further constructed a "collective pattern diagram" based on the probability maps for the individual patterns (see Fig. 4), in which the dominant collective pattern (as quantified by the emergence probability) for a given track width ω and Matrigel concentration ρ was selected for that set of (ω, ρ) (see Methods for details). In other words, this diagram shows the dominant invasion pattern (associated with the highest emergence probability) associated with a specific set of track widths and Matrigel concentrations. It can be clearly seen that the dominant pattern switched as the microenvironment factors changed. The four distinct regimes are identified in the diagram, corresponding to the four dominant invasion patterns: stream (red), blunt-tip (green), cone-tip (blue), and lumen (purple).

It is reasonable that on narrow tracks ($\omega < 26\,\mu$m), the stream pattern is the only pattern that emerged due to the strong geometric confinement, as the track width is roughly on the same order of magnitude as the linear size of a cell ($\sim$15 μm). The stream pattern remained dominant until $\omega\sim$26 μm (red domain in Fig. 4); then the blunt-tip pattern rapidly took over and became dominant for tracks with width varying from 40 μm to 100 μm. For large track widths, i.e., with ω between 100 μm and 176 μm, the blunt and stream patterns are dominant and compete with each other. The stream patterns show more advantage for high Matrigel concentration (>40%). For very wide tracks $\omega > 180\,\mu$m, all four patterns can emerge simultaneous and compete with one another, as the geometrical conferment due to track width is very weak for large ω. In this case, the effects of Matrigel concentration φ become prominence. For the very high concentration > 80%, the cone and blunt patterns dominate the region and compete with each other, while in the other range of concentration, the stream and lumen patterns become dominant. However, the cone-tip and lumen patterns exhibit strong advantages in extremely stiff ECM and extremely soft ECM, respectively.

The above results clearly demonstrate the significant impact of geometrical confinement (i.e., the track width) on collective migration dynamics and the emergence of different collective patterns of cancer cells. Moreover, the effects of Matrigel concentration were more significant for wide tracks, where the cells had more room to develop a richer spectrum of collective patterns, leading to the competition of various patterns on wider tracks. For a wide range of different microenvironmental conditions, the stream pattern shows a clear advantage, while the cone tip shows its advantage in the case of stiff ECM (i.e., high Matrigel density). The lumen pattern is dominant for large track widths and low Matrigel concentrations (i.e., soft ECM).

D. The collective migration speed and energy cost for invasion

To understand whether there is a physical advantage for certain collective invasion patterns, the migration speeds of the patterns were characterized while varying the track width and Matrigel concentration. The Matrigel layer affects the migration speed comparing with the tracks without Matrigel (see Fig. S4 [45]). A large variation in speeds was observed between the different patterns in the Matrigel microenvironment [Figs. 5(a)–5(d)], and even among the same patterns in the same track width and Matrigel concentration. No clear evidence was found that any of these patterns had an advantage with respect to migration speed because of the significant differences $p \gg 0.05$ among patterns at the same Matrigel concentration. Nevertheless, this might not be conclusive because the invasion-on-track experiments were limited by the relatively short time and space scale.

E. Mechanisms for the emergence of different collective migration patterns via cellular automaton simulations

Although the transition from stream to blunt-tip patterns as the track width increased is understandable, it is not immediately obvious why the cone-tip pattern became dominant only in the very wide tracks, or whether the cone-tip pattern provides any advantage to cancer cell invasion. To address these questions, the front speed of these invasion patterns was examined to determine whether there is any speed advantage associated with the cone-tip pattern. To our surprise, no significant difference in the invasion speed of the pattern types was found. In addition, the "energy cost" for Matrigel degradation (proportional to the total volume of Matrigel degraded during invasion) can be estimated when cancer cells collectively invade along the microtracks for the same distance. Results suggested that the energy cost is similar for both blunt-tip and cone-tip patterns, as the volume of ECM (i.e., Matrigel) degraded during invasion was the same in both cases regardless of the track width [Figs. 5(e) and 5(f)].

To further elucidate the mechanism behind the formation of various collective patterns, as well as to understand the transition of dominant patterns under different microenvironment constraints, we carried out extensive cellular automaton (CA) simulations. In our simulations, the tumor cells can possess distinct ECM degradation ability and motility due to cell-to-cell heterogeneity and can migrate on a geometrically confined microtrack covered by Matrigel. The CA rules are

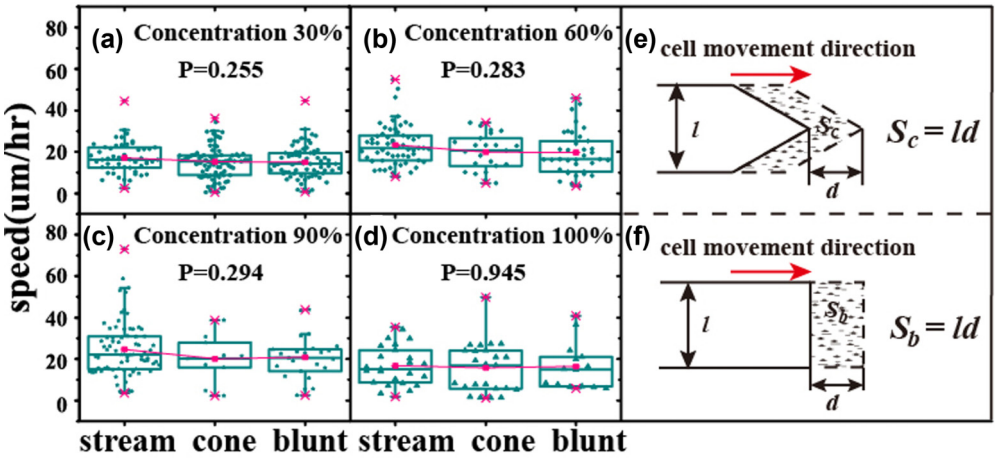

FIG. 5. Statistics of the speed at the invasive front of cancer cells. (a)–(d) The difference in speed according to pattern; the green points are the experimental data, and the pink line indicates the average speed. (e), (f) The energy cost in the cone-tip and blunt-tip patterns, d represents the movement distance of the collective cells via Matrigel degradation, l is the width of the collective cells. The red arrow shows the movement direction of collective cells. S_c and S_b (the shaded part surrounded by the dashed line) represent the area of the degraded Matrigel in the cone-tip and blunt-tip patterns, respectively. This assumes that the Matrigel is degraded by the high-activity cells or the leader of the collective cells. This shows that the area of S_c is equal to S_b, indicating no difference in energy cost in both cases along the same distance of invasion.

described in detail in the Methods section. We note that although all of our model parameters possess a clear physical interpretation, due to the model limitations, their values do not quantitatively correspond to the experimentally measured values. Nonetheless, our model provides qualitative insights on how geometrical constraint (i.e., track width) and migration resistance (i.e., Matrigel density) regulate the collective invasive behavior of the cells and give rise to various invasion patterns.

As shown in Fig. 6, all four of the experimentally observed steady-state collective migration patterns—multicellular stream, cone-tip, blunt-tip, and lumen patterns—were reproduced in our CA simulations. The simulated

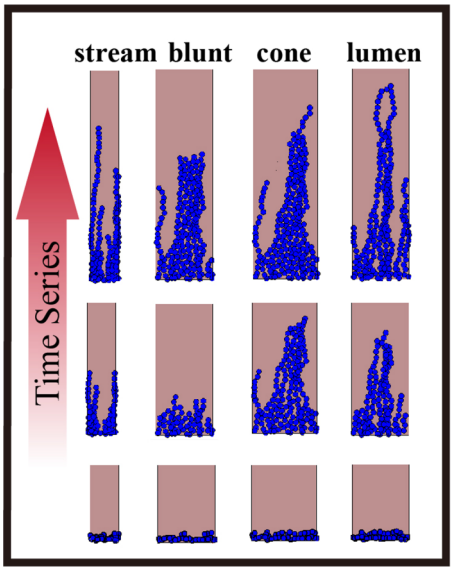

FIG. 6. Formation of distinct collective migration patterns associated with different microenvironmental factors (microtrack width and Matrigel density) via cellular automaton simulations.

multicellular stream patterns were typically associated with the narrow track width ($\omega < 25\,\mu$m) regardless of the Matrigel density ($0 < \rho < 1$), which is consistent with the corresponding experiments. Note that $\rho = 1$ indicates the maximal normalized Matrigel density, which is different from the experimental value and does not possess a physical unit. The range of the microenvironment parameters was consistent with the corresponding experimentally obtained values for which the stream pattern possessed the maximal probability of occurrence among all four of the patterns. The emergence probability of the four collective patterns obtained from CA simulations are shown in the supplemental tables S1–S4 [45]. The simulations revealed that in the early invasion stages, due to the geometrical constraint imposed by the narrow track, a small number of invasive cells migrated onto the Matrigel covered track, created individual invasion paths, and effectively became the leading cells. Once the subsequent follower cells found the paths created by the leading cell, they merged into the existing path due to the smaller resistance. These mechanisms eventually drove the cells to form the multicellular stream pattern, which is very stable on narrow tracks.

The simulated cone-tip patterns were typically associated with wide tracks ($\omega > 180\,\mu$m) and high Matrigel density ($\rho > 0.5$), which is consistent with the experimental results. In the large track width, many cells with invasion ability can migrate on the Matrigel-covered tracks during the initial stages to form a migration front. Due to the phenotypic heterogeneity among the tumor cells, the tumor cell with the strongest invasion ability (e.g., ECM degradation ability and motility in our model) begins to lead the invasion by creating an invasive path that deeply penetrates the dense Matrigel. Other cells originally on the invasion front subsequently follow this leading cell due to least-resistance path selection and the migration front eventually evolves into a stable cone-tip pattern. Therefore, the key mechanisms for the emergence of cone-tip patterns include large track widths, high

Matrigel resistance, and phenotypic heterogeneity among the cells.

The blunt-tip pattern was most commonly observed in the simulations with the track width in between the critical widths for the stream and cone-tip patterns. For the intermediate track widths and the low Matrigel resistance, the difference in the degradation capability may have a less significant effect on the migration dynamics. Multiple stream patterns emerged with similar invasion speeds during the initial stages and eventually merged to form a blunt pattern. Our simulation results allow us to construct a collective pattern diagram, which matches the experimentally obtained diagram very well.

Finally, the lumen pattern was observed in the very low density (i.e., $\rho < 0.25$) and the intermediate track widths, i.e., ω was between 150 μm and 200 μm, and these very rarely occurred. In the simulations, the lumen structure typically formed via the crossing over of two multicell streams, which was subsequently stabilized by cell-cell adhesion. Further collective migration with this lumen structure required that all of the cells forming the lumen possess roughly the same invasion ability and very low Matrigel resistance. Even in this case, small variation of the cellular invasion ability eventually led to instability and collapse of the lumen structure as the collective migration proceeded.

We note that the lumen patterns are commonly observed in clinical diagnosis (see Fig. 2), which is of direct relevance to the prognosis. Unfortunately, the procedure of lumen formation was not clear from our *in vitro* experiment. This is because the large high-resolution photos containing all tracks on the chip are stitched from several photos taken from microscope, and this technique cannot simultaneously guarantee both high spatial and temporal resolutions. We have chosen to maintain a high spatial resolution for accurately analyzing the morphology of different collective patterns and lost track of the detailed evolution of the patterns. Although our CA simulations can produce "lumen-like" patterns resulted from the merging of individual streaming pattern, this might not be the actual mechanism *in vivo* or *in vitro*. In future work, we will carry out a more systematic investigation to better understand the formation of lumen patterns.

IV. CONCLUSIONS AND DISCUSSION

In summary, we focused on the subtype of tumor morphology and found that the blunt tip of the collective invasion was more prevalent in breast cancer stages 2 and 3. To study the difference of the front patterns and the effects of the microenvironment on the front patterns, the "migration-on-chip" experiment was designed. We demonstrated, using "migration-on-chip" experiments and cellular automaton simulations, that the microenvironment can significantly influence the collective invasion or migration of cancer cells, giving rise to various collective migration patterns. We categorized the commonly observed collective patterns in pathological samples into four types: stream, blunt-tip, cone-tip, and lumen patterns. We designed and fabricated microchips containing high-throughput microscale tracks using protein repelling coating technology. By varying the geometric confinement (i.e., track width) and microenvironment factors (i.e., Matrigel concentration), we reproduced a diversity of *in vivo* collective migration patterns of invasive MDA-MB-231 breast cancer cells in the chips. We further quantified the emergence probability of each class of patterns as a function of microtrack width ω and Matrigel concentration ρ, and we devised a quantitative "collective pattern diagram" based on the dominant collective pattern for a given set of (ω, ρ). We also employed CA simulations to elucidate the mechanisms for the emergence of various collective patterns, incorporating the effects of both direct cell-cell interactions and microenvironment factors (e.g., chemical gradient and ECM degradation).

We found that although the stream patterns were dominant in the small track width, cone-tip patterns were commonly observed in the wide tracks. This is likely due to the operation of favorable invasive phenotype selection (e.g., ECM degradation ability), once the geometric confinement is not significant as the track width increases. Consequently, increasing Matrigel concentration can enhance the phenotype selection (or manifestation of phenotype heterogeneity), which leads to cone-tip patterns. Our CA simulation results also suggest that the phenotypic heterogeneity of invasive tumor cells and the selection of favorable phenotypes via tumor microenvironment interactions can be crucial to the collective migration patterns, especially in the case of cone-tip patterns. Heterogeneity is common in human cancers [50,51]. For example, significant differences in invasive phenotypes among individual tumor cells have been observed [50,52–54]. In addition, population heterogeneity also plays an important role in the emergence of drug resistance in cancer cells [55,56] and thus can significantly affect the outcome of chemotherapy [57]. It has also been suggested that tumor heterogeneity might be correlated with the level of malignancy [58–60]. In general, we expect that phenotypic heterogeneity in addition to the complex heterogeneous microenvironment would play a crucial role in giving rise to the collective invasion pattern *in vivo*.

Finally, we note that our high-throughput microchips, which allow one to investigate the effects of multiple microenvironmental factors on collective cell migration behavior, may also have potential applications in the study and classification of more complex invasion behaviors in metastatic cancers. Meanwhile, the immunofluorescence technique has been incorporated with the "migration on tracks" chip. In Ref. [9] the authors showed that high expression of Cytokeratin 14 is a significant signature of leading cells in cancer cell collective invasion. The protein Cytokeratin 14 also was stained using immunofluorescence technique in our platform. Our result in Ref. [45] shows that Cytokeratin 14 expression is higher in the leader cells than the follower cells, which is consistent with the results reported in Ref. [9] (see details in Fig. S5 [45]). In the *in vitro* experiment, to avoid the undesirable effects due to the inhomogeneity of collagen gels, Matrigel is used instead as the ECM in our experiments. However, the actual ECM *in vivo* is much more complex, containing various stromal cells and basal membrane, and therefore more challenging to be realistically mimicked using the current platform with Matrigel. In such case, the Matrigel layer could be replaced by a collagen layer with stromal cells embedded. The invasive tumor cells can also be cocultured with non-metastatic cells, such as MCF-7 or MCF-10A, to investigate

the effects of intercellular adhesion on collective cellular behaviors.

ACKNOWLEDGMENTS

This work was supported by the National Natural Science Foundation of China (Grants No. 11474345, No. 11674043, and No. 11604030), Fundamental Research Funds for the Central Universities (2018CDJDWL0011), Fundamental and Advanced Research Program of Chongqing (Grant No. cstc2018jcyjAX0338), China, Arizona State University Graduate Fellowships, and Arizona State University start-up funds, USA.

[1] Y. Kienast *et al.*, Real-time imaging reveals the single steps of brain metastasis formation, Nature Med. **16**, 116 (2010).
[2] J. J. Christiansen and A. K. Rajasekaran, Reassessing epithelial to mesenchymal transition as a prerequisite for carcinoma invasion and metastasis, Cancer Res. **66**, 8319 (2006).
[3] P. Friedl *et al.*, Classifying collective cancer cell invasion, Nature Cell Biol. **14**, 777 (2012).
[4] M. Díaz-Núñez *et al.*, Histone deacetylase inhibitors induce invasion of human melanoma cells in vitro via differential regulation of N-cadherin expression and RhoA activity, BMC Cancer **16**, 667 (2016).
[5] E. Dona *et al.*, Directional tissue migration through a self-generated chemokine gradient, Nature (London) **503**, 285 (2013).
[6] S. A. Godinho *et al.*, Oncogene-like induction of cellular invasion from centrosome amplification, Nature (London) **510**, 167 (2014).
[7] M. S. Hutson *et al.*, Forces for morphogenesis investigated with laser microsurgery and quantitative modeling, Science **300**, 145 (2003).
[8] K. J. Cheung and A. J. Ewald, Illuminating breast cancer invasion: Diverse roles for cell-cell interactions, Curr. Opin. Cell Biol. **30**, 99 (2014).
[9] K. J. Cheung *et al.*, Collective invasion in breast cancer requires a conserved basal epithelial program, Cell **155**, 1639 (2013).
[10] A. Cliffe *et al.*, Quantitative 3D analysis of complex single border cell behaviors in coordinated collective cell migration, Nature Commun. **8**, 14905 (2017).
[11] T. Das and J. P. Spatz, Getting a grip on collective cell migration, Nature Cell Biol. **18**, 1264 (2016).
[12] D. Stichel *et al.*, An individual-based model for collective cancer cell migration explains speed dynamics and phenotype variability in response to growth factors, NPJ Syst. Biol. Appl. **3**, 5 (2017).
[13] A. Szabo and R. Mayor, Cell traction in collective cell migration and morphogenesis: The chase and run mechanism, Cell Adhes. Migr. **9**, 380 (2015).
[14] K. Matsushita, Cell-alignment patterns in the collective migration of cells with polarized adhesion, Phys. Rev. E **95**, 032415 (2017).
[15] O. Donnez *et al.*, Invasion process of induced deep nodular endometriosis in an experimental baboon model: Similarities with collective cell migration? Fertility Sterility **104**, 491 (2015).
[16] M. Egeblad and Z. Werb, New functions for the matrix metalloproteinases in cancer progression, Nature Rev. Cancer **2**, 161 (2002).
[17] X. X. He, B. Lee, and Y. Jiang, Cell-ECM interactions in tumor invasion: Systems biology of tumor microenvironment, Quant. Model. Sim. **936**, 73 (2016).
[18] M. Picchio *et al.*, Intratumoral spatial distribution of hypoxia and angiogenesis assessed by F-18-FAZA and I-125-gluco-RGD autoradiography, J. Nuclear Med. **49**, 597 (2008).
[19] I. M. Shapiro *et al.*, An EMT-driven alternative splicing program occurs in human breast cancer and modulates cellular phenotype, PLoS Genetics **7**, e1002218 (2011).
[20] K. Wolf *et al.*, Compensation mechanism in tumor cell migration: Mesenchymal-amoeboid transition after blocking of pericellular proteolysis, J. Cell Biol. **160**, 267 (2003).
[21] T. S. Deisboeck and I. D. Couzin, Collective behavior in cancer cell populations, Bioessays **31**, 190 (2009).
[22] P. Friedl and D. Gilmour, Collective cell migration in morphogenesis, regeneration and cancer, Nature Rev. Mol. Cell Biol. **10**, 445 (2009).
[23] P. Friedl and S. Alexander, Cancer invasion and the microenvironment: Plasticity and reciprocity, Cell **147**, 992 (2011).
[24] A. Albini and M. B. Sporn, The tumour microenvironment as a target for chemoprevention, Nature Rev. Cancer **7**, 139 (2007).
[25] A. D. Doyle *et al.*, One-dimensional topography underlies three-dimensional fibrillar cell migration, J. Cell Biol. **184**, 481 (2009).
[26] M. Ghibaudo *et al.*, Substrate topography induces a crossover from 2D to 3D behavior in fibroblast migration, Biophys. J. **97**, 357 (2009).
[27] C. D. Paul *et al.*, Engineered models of confined cell migration, Annu. Rev. Biomed. Eng. **18**, 159 (2016).
[28] M. Poujade *et al.*, Collective migration of an epithelial monolayer in response to a model wound, Proc. Natl. Acad. Sci. USA **104**, 15988 (2007).
[29] H. G. Yevick *et al.*, Architecture and migration of an epithelium on a cylindrical wire, Proc. Natl. Acad. Sci. USA **112**, 5944 (2015).
[30] C. S. Chen *et al.*, Using self-assembled monolayers to pattern ECM proteins and cells on substrates, Methods Mol. Biol. **139**, 209 (2009).
[31] C. D. Paul, P. Mistriotis, and K. Konstantopoulos, Cancer cell motility: Lessons from migration in confined spaces, Nature Rev. Cancer **17**, 131 (2017).
[32] A. M. Fuzer *et al.*, Effects of limonoid cedrelone on MDA-MB-231 breast tumor cells in vitro, Anti-Cancer Agents Med. Chem. **13**, 1645 (2013).
[33] E. R. Geisbrecht *et al.*, Genetic interaction screens identify a role for hedgehog signaling in *Drosophila* border cell migration, Dev. Dyn. **242**, 414 (2013).
[34] J. P. Kaiser, A. Reinmann, and A. Bruinink, The effect of topographic characteristics on cell migration velocity, Biomaterials **27**, 5230 (2006).
[35] C. C. Berry *et al.*, The influence of microscale topography on fibroblast attachment and motility, Biomaterials **25**, 5781 (2004).

[36] D. E. Discher, P. Janmey, and Y. L. Wang, Tissue cells feel and respond to the stiffness of their substrate, Science **310**, 1139 (2005).

[37] M. T. Frey *et al.*, Cellular responses to substrate topography: Role of myosin II and focal adhesion kinase, Biophys. J. **90**, 3774 (2006).

[38] T. Tzvetkova-Chevolleau *et al.*, The motility of normal and cancer cells in response to the combined influence of the substrate rigidity and anisotropic microstructure, Biomaterials **29**, 1541 (2008).

[39] V. Vogel and M. Sheetz, Local force and geometry sensing regulate cell functions, Nature Rev. Mol. Cell Biol. **7**, 265 (2006).

[40] A. Tourovskaia, X. Figueroa-Masot, and A. Folch, Long-term microfluidic cultures of myotube microarrays for high-throughput focal stimulation, Nature Protoc. **1**, 1092 (2006).

[41] W. Han *et al.*, Oriented collagen fibers direct tumor cell intravasation, Proc. Natl. Acad. Sci. USA **113**, 11208 (2016).

[42] P. Diamandis and K. Aldape, World Health Organization classification of central nervous system tumors, Neurol. Clinics **36**, 439 (2018).

[43] A. P. Stout, The atlas of tumor pathology, Am. J. Clin. Pathol. **25**, 175 (1955).

[44] K. Washington, 7th edition of the AJCC Cancer Staging Manual: Stomach, Ann. Surg. Oncol. **17**, 3077 (2010).

[45] See Supplemental Material at http://link.aps.org/supplemental/10.1103/PhysRevE.99.062403 for additional information including movies to help understand this article.

[46] Y. Jiao and S. Torquato, Emergent behaviors from a cellular automaton model for invasive tumor growth in heterogeneous microenvironments, PLoS Comput. Biol. **7**, e1002314 (2011).

[47] Y. Jiao and S. Torquato, Evolution and morphology of microenvironment-enhanced malignancy of three-dimensional invasive solid tumors, Phys. Rev. E **87**, 052707 (2013).

[48] Y. Jiao and S. Torquato, Diversity of dynamics and morphologies of invasive solid tumors, AIP Adv. **2**, 011003 (2012).

[49] J. R. Zhu *et al.*, Enhanced invasion of metastatic cancer cells via extracellular matrix interface, PLoS ONE **10**, e0118058 (2015).

[50] S. P. Carey *et al.*, Leading malignant cells initiate collective epithelial cell invasion in a three-dimensional heterotypic tumor spheroid model, Clin. Exp. Metastasis **30**, 615 (2013).

[51] E. V. Denisov *et al.*, Clinically relevant morphological structures in breast cancer represent transcriptionally distinct tumor cell populations with varied degrees of epithelial-mesenchymal transition and CD44+CD24- stemness, Oncotarget **8**, 61163 (2017).

[52] J. Konen *et al.*, Image-guided genomics of phenotypically heterogeneous populations reveals vascular signalling during symbiotic collective cancer invasion, Nat. Commun. **8**, 15078 (2017).

[53] L. Liu *et al.*, Minimization of thermodynamic costs in cancer cell invasion, Proc. Natl. Acad. Sci. USA **110**, 1686 (2013).

[54] A. Chapman *et al.*, Heterogeneous tumor subpopulations cooperate to drive invasion, Cell Rep. **8**, 688 (2014).

[55] E. V. Denisov *et al.*, Invasive and drug resistant expression profile of different morphological structures of breast tumors, Neoplasma **62**, 405 (2015).

[56] N. C. Turner and J. S. Reis, Genetic heterogeneity and cancer drug resistance, Lancet Oncol. **13**, E178 (2012).

[57] R. Buetof, A. Dubrovska, and M. Baumann, Clinical perspectives of cancer stem cell research in radiation oncology, Radiother. Oncol. **108**, 388 (2013).

[58] M. R. Lindberg, *Diagnostic Pathology: Soft Tissue Tumors*, 2nd ed. (Elsevier, Philadelphia, PA, 2015).

[59] P. Gattuso, V. B. Reddy, O. David *et al.*, *Differential Diagnosis in Surgical Pathology* (Saunders/Elsevier, Philadelphia, PA, 2010), pp. 191–193.

[60] W. M. Cong, *Surgical Pathology of Hepatobiliary Tumors* (Springer, Singapore, 2017), pp. 128–131.